

# On the time evolution of climate sensitivity and future warming

2

Philip Goodwin<sup>1</sup>

4

<sup>1</sup> *Ocean and Earth Sciences, University of Southampton, Southampton, UK*

6

P. Goodwin, ORCID ID: <https://orcid.org/0000-0002-2575-8948>

8

Manuscript re-submitted to *Earth's Future*

10

16<sup>th</sup> July 2018

12

Accepted for publication in *Earth's Future*

6<sup>th</sup> September 2018

14

This is the Author Accepted Manuscript

16

20 The Earth's climate sensitivity to radiative forcing remains a key source of uncertainty in  
21 future warming projections. There is a growing realisation in recent literature that research  
22 must go beyond an equilibrium and CO<sub>2</sub>-only viewpoint, towards considering how climate  
23 sensitivity will evolve over time in response to anthropogenic and natural radiative forcing  
24 from multiple sources. Here, the transient behaviour of climate sensitivity is explored using a  
25 modified energy balance model, in which multiple climate feedbacks evolve independently  
26 over time to multiple sources of radiative forcing, combined with constraints from  
27 observations and from the Climate Model Intercomparison Project phase 5 (CMIP5). First, a  
28 large initial ensemble of 10<sup>7</sup> simulations is generated, with a distribution of climate feedback  
29 strengths from sub-annual to 10<sup>2</sup> year timescales constrained by the CMIP5 ensemble;  
30 including the Planck feedback, the combined water-vapour lapse-rate feedback, snow and  
31 sea-ice albedo feedback, fast cloud feedbacks, and the cloud response to SST-adjustment  
32 feedback. These 10<sup>7</sup> simulations are then tested against observational metrics representing  
33 decadal trends in warming, heat and carbon uptake, leaving only 4.6×10<sup>3</sup> history-matched  
34 simulations consistent with both the CMIP5 ensemble and historical observations. The results  
35 reveal an annual-timescale climate sensitivity of 2.1 °C (ranging from 1.6 to 2.8 °C at 95%  
36 uncertainty), rising to 2.9 °C (from 1.9 to 4.6 °C) on century timescales. These findings  
37 provide a link between lower estimates of climate sensitivity, based on the current transient  
38 state of the climate system, and higher estimates based on long-term behaviour of complex  
39 models and palaeoclimate evidence.

40

## 42 1. Introduction

43 There is currently significant uncertainty in the sensitivity of Earth's climate to radiative  
44 forcing, with the IPCC Assessment Report 5 (IPCC, 2013) estimating that the Equilibrium  
45 Climate Sensitivity (ECS, measuring the surface temperature response in °C to a sustained  
46 doubling of CO<sub>2</sub>) ranges from 1.5 °C to 4.5 °C (Fig. 1a, black). This 1.5 to 4.5 °C range from  
47 IPCC (2013) incorporates many separate estimates of the ECS that have been made from  
48 multiple lines of evidence (e.g. see Knutti et al., 2017 see Figure 2 therein). Now consider a  
49 small selection of estimates chosen to reflect evidence from current energy budgets, complex  
50 Earth system models, and modern and geological observations. Estimates from energy  
51 balance considerations of the current transient climate system (Otto et al., 2013; Lewis and  
52 Curry et al., 2014) imply a best estimate ECS towards the lower end of the IPCC range (Fig.  
53 1a, dark gray) of circa 1.6 to 2 °C. In contrast, analysis of the century timescale ECS from  
54 observation-constrained climate models (Cox et al., 2018), or from a combination of  
55 observational and geological constraints (Goodwin et al., 2018), suggests best estimate values  
56 from the middle of the IPCC range (Fig. 1a, light grey) of circa 3 °C. Together with this  
57 uncertainty in the value of the ECS is a growing acknowledgement that the Earth's climate  
58 sensitivity is likely to evolve through time, both due to time-evolving processes included  
59 within climate models (Armour et al., 2013; Knutti and Rugenstein, 2017; Williams et al.,  
60 2008; Andrews et al., 2015; Caldwell et al., 2016; Figure 2a), and over longer geological  
61 timescales (Zeebe, 2013; Rohling et al, 2018).

62

63 In a simple 1-dimensional energy balance model, the global mean surface warming at time  $t$ ,  
64  $\Delta T(t)$  in °C, is empirically linked to the difference between total radiative forcing,  $R_{total}(t)$  in

66  $\text{Wm}^{-2}$ , and the Earth's net energy imbalance,  $N(t)$  in  $\text{Wm}^{-2}$ , via an effective climate feedback  
parameter,  $\lambda$  in  $\text{Wm}^{-2}\text{K}^{-1}$ , via

68 
$$\lambda\Delta T(t) = R_{total}(t) - N(t), \quad (1)$$

70 where, the total radiative forcing is a sum from  $i$  independent sources,  $R_{total}(t) = \sum_i R_i(t)$ , and  
72 the effective climate feedback parameter is defined such that  $\lambda\Delta T(t)$  represents the total  
aggregated outgoing radiative response in  $\text{Wm}^{-2}$  to the surface warming accounting for all  
74 feedback processes. Note that the word 'effective' is used here to suggest that the value of the  
climate feedback may represent an aggregated response, composed of different climate  
76 feedback values relating to different sources of radiative forcing, that may be changing  
through time.

78 However, there are a number of important deficiencies in this approach, which have been  
illustrated by applying this equation to the output of complex climate models. Firstly, the  
80 effective climate feedback parameter,  $\lambda$ , is not expected to remain constant in time, but  
instead display transient behaviour as different climate feedbacks respond to the imposed  
82 forcing over different timescales (e.g. Andrews and Webb, 2018; Caldwell et al. 2016; Knutti  
& Rugenstein, 2017; Zeebe, 2013; PALAEOSENS, 2012; Rohling et al., 2018; Senior and  
84 Mitchell, 2000; Gregory et al., 2004; Williams et al., 2008; Armour et al., 2013; Paynter et  
al., 2018; see Figure 2a). Secondly,  $\lambda$  may be different for different sources of radiative  
86 forcing, potentially arising due to the different spatial patterns of radiative forcing from  
different agents (Hansen et al. 2005; Marvel et al., 2016; Gregory and Andrews, 2016).  
88 Thirdly, in some models the ocean heat uptake (the dominant component of  $N$ ), can have a  
larger effect on warming during transient climate change than an equivalent magnitude of  
90 radiative forcing,  $R$ , (e.g. Winton et al., 2010; Geoffroy et al., 2013; Frölicher et al., 2014).

92 Potentially, the discrepancy between climate sensitivity estimates derived from the Earth's  
current transient state energy balance (Otto et al, 2013; Lewis and Curry, 2014) and climate  
94 sensitivity estimates for century timescales (Cox et al., 2018; Goodwin et al., 2018) may be  
linked to the deficiencies in equation (1) (Fig. 1, compare dark and light gray). For example,  
96  $\lambda$  may change over time between the current transient state and century timescales, the spatial  
pattern of radiative forcing and relative contributions from each agent today may not apply in  
98 the future, and the large current value of  $N$  in the current transient state may reduce as the  
system approaches a new steady state.

100

Without explicitly putting a time-dependence on the climate feedback, the simple 1-  
102 dimensional energy balance model (1) has been extended (e.g. Hansen et al., 2005; Winton et  
al, 2010; Geoffroy et al., 2013; Frölicher et al., 2014; Marvel et al., 2016; Goodwin et al.,  
104 2015) by considering non-dimensional efficacy weighting on both the contributions to  
radiative forcing,  $\varepsilon_i$ , and the Earth's energy imbalance,  $\varepsilon_N$ , via,

106

$$\lambda\Delta T(t) = R_{total}^{weighted}(t) - \varepsilon_N N(t), \quad (2)$$

108

110 where the total efficacy weighted radiative forcing at time  $t$  is the sum of contributions from  $i$   
independently time-varying sources with each contribution weighted by a non-dimensional

efficacy term  $\varepsilon_i$ ,  $R_{total}^{weighted}(t) = \sum_i \varepsilon_i R_i(t)$  (Marvel et al., 2015), and  $\varepsilon_N N(t)$  in  $\text{Wm}^{-2}$  represents

112 the total efficacy-weighted energy imbalance of the Earth system.

114 Goodwin et al. (2018) utilised this extended 1-dimensional energy balance model (2), with  
 115 efficacy-weighting but with climate feedback assumed constant in time, to drive an efficient  
 116 Earth system model, generating history-matched projections of future warming and  
 117 constraining century-timescale climate sensitivity (Fig. 1a, light gray). Instead of applying  
 118 efficacy weightings (2), this study explores an alternative approach: Here, the energy balance  
 119 equation (1) is extended to explicitly include time-varying climate feedbacks from multiple  
 120 processes, that each respond independently to multiple radiative forcing agents. This  
 121 extended energy balance equation is then used to constrain the climate sensitivity over  
 122 multiple timescales, and used to show that this may explain the discrepancy between climate  
 123 sensitivity estimates from the current transient energy balance and century timescale  
 124 approaches (Fig. 1).

126 Section 2 derives the extended 1-dimensional energy balance model with  $j$  climate feedbacks  
 127 independently responding over time to  $i$  radiative forcing agents. Section 3 then describes  
 128 how the Warming Acidification and Sea level Projector (WASP) model (Goodwin, 2016;  
 129 Goodwin et al., 2018) is extended to incorporate this extended energy balance equation and  
 130 used to perform a large ensemble of climate simulations, where the initial distributions for the  
 131 climate feedback strengths for the  $j$  processes are taken from the range of feedback strengths  
 132 in the CMIP5 model ensemble analysed by Caldwell et al. (2016) and Andrews et al. (2015).  
 133 A history matching approach (Williamson et al., 2015) is then applied, after Goodwin et al.  
 134 (2018), to extract combinations of feedback strengths that are consistent with observational  
 135 constraints (Table 2) for surface warming (Morice et al., 2012; GISSTEMP, 2018; Hansen et  
 136 al, 2010; Smith et al., 2008; Vose et al., 2012), ocean heat uptake (Levitus et al., 2012; Giese  
 137 et al., 2011; Balmeseda et al., 2013; Good et al., 2013; Smith et al., 2015; Cheng et al., 2017;  
 138 Kennedy et al., 2011; Huang et al., 2015) and carbon fluxes (IPCC, 2013 for 90% confidence  
 139 bounds, based on original data now summarized in Le Quéré et al., 2018). Section 4 presents  
 140 the history-matched results, evaluating the timescale evolutions of climate feedback, climate  
 141 sensitivity and future warming that are consistent with observational and CMIP5 constraints.  
 142 Section 5 discusses the wider implications of this study.

## 144 2. Time-evolving climate feedbacks

145 Consider a climate system where there are  $i$  independently time-varying sources of radiative  
 146 forcing,  $R_i(t)$  in  $\text{Wm}^{-2}$ , such that the total radiative forcing is written,

$$148 \quad R_{total}(t) = \sum_i R_i(t). \quad (3)$$

150 The  $i$  different sources of radiative forcing include radiative forcing from atmospheric  $\text{CO}_2$ ,  
 151 other well-mixed greenhouse gases such as methane and nitrous oxide, solar forcing, and  
 152 spatially localised forcing such as tropospheric aerosols and volcanic stratospheric aerosols  
 153 (Figure 3).

154 In response to each of the  $i$  source of radiative forcing there are  $j$  independently time-  
 155 evolving climate feedback processes,  $\lambda_{i,j}(t)$  in  $\text{Wm}^{-2} \text{K}^{-1}$ , such that the total climate feedback  
 156 due to radiative forcing agent  $i$  is written

$$160 \quad \lambda_i(t) = \lambda_{Planck} + \sum_j \lambda_{i,j}(t), \quad (4)$$

162 where  $\lambda_{Planck}$  is the Planck sensitivity, equal to around  $3.15 \text{ Wm}^{-2} \text{ K}^{-1}$  (Caldwell et al., 2016)  
 163 and  $\lambda_{i,j}(t)$  is the climate feedback from process  $j$  in response to forcing agent  $i$ . The  $j$  climate  
 164 feedback processes include the combined water vapour – lapse rate feedback, fast cloud  
 165 feedbacks, snow and sea-ice albedo feedbacks, and the slow cloud feedback occurring as the  
 166 spatial pattern of SSTs change in response to warming over many decades (Figure 2a). These  
 167 feedbacks from the  $j$  processes operate over a range of different timescales. For example, it  
 168 takes order 10 days for water vapour to respond to surface warming, but due to the presence  
 169 of multi-year sea ice it may take years for the snow + sea-ice albedo to respond to an imposed  
 170 forcing, while it may take many decades for SST warming patterns to adjust towards an  
 171 equilibrium state, thereby altering cloud feedback (Andrews et al., 2015).

172 The aim is to derive a modified energy balance equation that solves for the global mean  
 173 surface temperature anomaly over time,  $\Delta T(t)$ , explicitly accounting for the independence of  
 174 the  $j$  climate feedback responses to each of the  $i$  sources of radiative forcing. First, the  
 175 general 1-D energy balance equation, (1), is re-arranged to solve for warming in terms of the  
 176 ratio of the total radiative forcing  $R_{total}(t)$  (Figure 3b) to the overall effective climate feedback  
 177  $\lambda(t)$ ,

$$180 \quad \Delta T(t) = \left(1 - \frac{N(t)}{R_{total}(t)}\right) \left(\frac{R_{total}(t)}{\lambda(t)}\right). \quad (5)$$

182 Next, we notice from (5) that the total radiative forcing divided by the overall effective  
 183 climate feedback parameter at time  $t$ ,  $R_{total}(t)/\lambda(t)$ , represents the overall warming that would  
 184 be achieved from all sources of radiative forcing if the global climate system were in energy  
 185 balance,  $N(t) = 0$ , via

$$188 \quad \Delta T|_{N(t)=0}(t) = \left(\frac{R_{total}(t)}{\lambda(t)}\right). \quad (6)$$

190 We now state, by definition, that the radiative forcing from the  $i$ th agent divided by the  
 191 climate feedback parameter for the  $i$ th agent at time  $t$ ,  $R_i(t)/\lambda_i(t)$ , similarly represents the  
 192 warming that would be achieved from radiative forcing by the  $i$ th agent if the global energy  
 193 system were brought into balance,  $N(t) = 0$ , via

$$194 \quad \Delta T_i|_{N(t)=0}(t) = \left(\frac{R_i(t)}{\lambda_i(t)}\right). \quad (7)$$

196 Now, it is assumed that the radiative forcing from all  $i$  sources is separable. This is  
 197 reasonable if either the  $i$  sources of radiative forcing affect the absorption of different  
 198 radiation wavelengths, or the absorption of radiation at a given wavelength by one agent is  
 199 independent of the absorption at the same wavelength by another. Note that while the  
 200 radiative forcing from  $\text{CH}_4$  and  $\text{N}_2\text{O}$  do have a dependence upon one another (Myhre et al,

202 2013), for the WASP experiments here these terms are combined into a single source of  
 204 radiative forcing representing all greenhouse gases other than CO<sub>2</sub> (Figure 3, blue), which  
 can be considered separable from the other agents.

206 Under the separable radiative forcing assumption for the  $i$  agents, the total warming from all  
 208 sources of radiative forcing if the system is brought into energy balance must be equal to the  
 sum of warming contributions from all  $i$  sources of radiative forcing at energy balance,

$$\sum_i \Delta T_i \Big|_{N(t)=0} (t) = \Delta T \Big|_{N(t)=0} (t). \text{ This allows us to write from (6) and (7),}$$

210

$$212 \quad \sum_i \left[ \frac{R_i(t)}{\lambda_i(t)} \right] = \frac{R_{total}(t)}{\lambda(t)}. \quad (8)$$

214 Substituting (8) into (5) gives an expression for global mean surface warming at time  $t$  as a  
 216 function of the separate radiative forcing and climate feedback parameters for the  $i$  forcing  
 agents,

$$218 \quad \Delta T(t) = \left( 1 - \frac{N(t)}{R_{total}(t)} \right) \sum_i \left[ \frac{R_i(t)}{\lambda_i(t)} \right], \quad (9)$$

220 The total modified energy balance equation for global mean surface warming from  $j$  climate  
 222 feedback processes, which each evolve independently in response to  $i$  radiative forcing  
 agents, is found by substituting (4) into (9) to reveal,

$$224 \quad \Delta T(t) = \left( 1 - \frac{N(t)}{R_{total}(t)} \right) \sum_i \left[ \frac{R_i(t)}{\lambda_{Planck} + \sum_j \lambda_{i,j}(t)} \right]. \quad (10)$$

226 Note that the total warming from the  $i$  different forcing agents when  $N \neq 0$  is not equal to the  
 228 sum of warming if each of the  $i$  agents acted alone in this energy balance equation, (10). This  
 is because the ratio  $N(t)/R_{total}(t)$  in equation (10) evolves according to the combined history of  
 radiative forcing from all forcing agents, and would be different for the individual forcing  
 230 agents acting alone (Figure 3).

232 The next section applies this energy balance equation (10), with independently time-varying  
 forcing and feedbacks, to drive the efficient WASP Earth system model (Goodwin, 2016;  
 234 Goodwin et al., 2018).

### 236 **3. Numerical Earth system model with modified energy balance equation**

WASP (Goodwin, 2016; Goodwin et al., 2018) is an efficient Earth system model that solves  
 238 for global mean surface warming for carbon emissions scenarios using an energy balance  
 equation with coupled carbon cycle terms (Goodwin et al., 2015). The WASP configuration  
 240 of Goodwin et al. (2018) assumed a constant value for the effective climate feedback over  
 time,  $\lambda$ , and applied non-dimensional efficacy weightings to heat uptake,  $N$ , and to the  
 242 radiative forcing from aerosols,  $R_{aerosol}$ , equation (2). Here, we modify the WASP model by  
 solving for global mean surface warming using equation (10), allowing climate feedback to

244 vary over time independently for each forcing agent, and removing the non-dimensional  
245 efficacy weightings for heat imbalance and the different sources of radiative forcing.

246

### 3.1 Time dependent climate feedbacks in WASP

248 This section, and Appendix A, present the alterations made to the WASP model configuration  
249 of Goodwin et al. (2018) to enable warming to be calculated via equation (10). The full code  
250 for this version of the WASP model is available in Supplementary Information.

252 Consider a step function in the radiative forcing from agent  $i$  at time  $t=t_0$ ,  $R_i(t \geq t_0) \neq 0$ , where  
253  $R_i(t < t_0) = 0$ . Initially, at time  $t=t_0$  the climate feedback to agent  $i$  is given by the Planck  
254 feedback,  $\lambda_i(t=t_0) = \lambda_{Planck}$ . Here, we assume that the climate feedback contributions from the  
255  $j$  climate processes then evolve towards their equilibrium values,  $\lambda_{i,j}^{equil}$ , with e-folding  
256 timescales for each process,  $\tau_j$ . Thus, the overall climate feedback parameter, following a  
257 step-function for the  $i$ th source of radiative forcing, from all  $j$  processes at time  $t_0 + \Delta t$ ,  
258  $\lambda_i(t_0 + \Delta t)$ , becomes,

$$260 \quad \lambda_i(t_0 + \Delta t) = \sum_j \lambda_{i,j}^{equil} \left( 1 - \exp\left(\frac{-\Delta t}{\tau_j}\right) \right). \quad (11)$$

262 In the general case radiative forcing from each agent does not increase via a step function, but  
263 instead by pathways that can increase or decrease over time (Figure 3a). This is achieved in  
264 WASP by using two time-stepping equations (see Appendix): one equation adjusting the  
265 climate feedbacks to the existing radiative forcing to the  $i$ th source at the previous time-step,  
266 and a second equation adjusting the climate feedback to the additional radiative forcing from  
267 the  $i$ th source since the previous time-step, to account for the feedback to any additional  
268 radiative forcing being the Planck feedback initially. Full details are given in the Appendix.

270 Other alterations to the WASP model, from the configuration of Goodwin et al. (2018),  
271 include:

272 (1) the time-step is reduced from 1/12<sup>th</sup> of a year to 1/48<sup>th</sup> of a year (Appendix A), and  
273 (2) the equations calculating the heat imbalance,  $N$  (see Goodwin, 2016; equations 3 and 4  
274 therein), are altered to reflect the multiple time-varying climate feedback terms in (10)  
(Appendix A).

276

277 Separate radiative forcing terms from CO<sub>2</sub>, other Well Mixed Greenhouse Gasses (WMGHG)  
278 and tropospheric aerosols are retained from the configuration of Goodwin et al. (2018)  
279 (Figure 3a), after Meinshausen et al. (2011), while solar radiative forcing (Meinshausen et al.  
280 2011) and volcanic radiative forcing (from NASA GISS record,  
<https://data.giss.nasa.gov/modelforce/strataer/>; see Bouassa et al., 2012) are added (Figure  
281 3a). The volcanic radiative forcing is added using the NASA record of Aerosol Optical Depth  
282 (AOD) since 1850 and applying a multiplier of  $-19 \pm 0.5 \text{ Wm}^{-2}$  per unit AOD (Gregory et al.,  
283 2016), where the uncertainty represents the standard deviation of the multiplier between the  
284 different models in the ensemble. Where the time-resolution of radiative forcing (or  
285 atmospheric composition) is less than 1/48<sup>th</sup> of a year, the values are linearly interpolated  
286 between time-steps.

288

### 3.2 Generating an ensemble constrained by observations and CMIP5

290 This section details the construction of the very large initial Monte Carlo model ensemble,  
291 and the subsequent history matching used to extract the smaller final ensemble of constrained

292 model simulations. First, an initial ensemble of  $10^7$  simulations is generated with the strength  
of climate feedback from different processes taken from analysis of CMIP5 models by  
294 Caldwell et al. (2016) and Andrews et al. (2015) (Table 1; Figure 2a). All other model  
parameters are varied with input distributions after the configuration of Goodwin et al. (2018  
296 – see Supplementary Table 2 therein).

298 The random-normal input distributions of climate feedback at equilibrium from Planck  
feedback,  $\lambda_{Planck}$ , combined Water Vapour Lapse Rate (WVLR),  $\lambda_{WVLR}$ , fast cloud adjustment,  
300  $\lambda_{FastCloud}$  and albedo adjustment,  $\lambda_{albedo}$ , (Table 1) are taken from analysis of these feedbacks  
in CMIP5 models by Caldwell et al (2016). The random-normal input distribution of climate  
302 feedback at equilibrium from the SST warming pattern adjustment-cloud feedback,  $\lambda_{SlowCloud}$ ,  
is taken from the change in cloud feedback over time in CMIP5 models analysed by Andrews  
304 et al. (2015). These feedbacks are imposed with different input distributions for the  
timescales,  $\tau_j$  (Table 1), with  $\lambda_{Planck}$  assumed to act instantaneously in all model simulations  
306 (Table 1).

308 The timescales for water-vapour lapse rate,  $\tau_{WVLR}$ , and fast cloud feedback,  $\tau_{FastCloud}$ , are  
varied with random-normal input distributions set to the residence time of water vapour in the  
310 atmosphere of  $8.8 \pm 0.4$  days (Ent and Tuinenburg, 2017). The global surface albedo feedback  
is found by Colman (2013) to have components acting from seasonal up to decadal  
312 timescales, presumably reflecting fast snow responses up to slower multi-year sea-ice  
responses. To simulate this range, the timescale for the snow and sea-ice albedo feedback,  
314  $\tau_{albedo}$ , is varied with a random distribution between 0.5 and 5 years (Table 1). The timescale  
for the slow cloud-SST adjustment feedback,  $\tau_{SlowCloud}$ , is varied with a random distribution  
316 from 20 to 45 years. The lower limit of 20 years is set by the initial time window Andrews et  
al. (2015) used to assess the response of CMIP5 models before the  $\lambda_{SlowCloud}$  feedback  
318 applied. The upper limit of 45 years is (1) set to ensure that there are enough e-folding  
timescales for the  $\lambda_{SlowCloud}$  feedback to take effect in the CMIP5 model simulations analysed  
320 by Andrews et al. (2015), and (2) set equal to a timescale for the thermocline identified by  
Fine et al. (2017), since spatial adjustment of SST warming patterns is likely linked to  
322 adjustments within the thermocline.

324 The combination of input distributions for feedback strengths,  $\lambda_{i,j}$ , and timescales,  $\tau_j$ , (Table  
1) results in a wide range of climate feedback over time in the initial  $10^7$ -simulation ensemble  
326 (Figure 2b, gray).

328 The same values of climate feedback at equilibrium from each process are applied here to  
each source of radiative forcing (Table 1), except that the snow and sea-ice albedo feedback  
330 is reduced to 20% for volcanic stratospheric aerosol forcing compared to the other sources of  
radiative forcing (Table 1). This reflects the finding by Gregory et al. (2016) that in a CMIP5  
332 model volcanic aerosols cause around 1.4 times less warming or cooling than an equivalent  
radiative forcing from  $\text{CO}_2$ . Here, this is imposed in the model by reducing the snow and sea  
334 ice albedo feedback term for volcanic aerosols, because the majority of volcanic forcing  
occurs at low latitudes and the majority of snow and sea-ice albedo forcing occurs at high  
336 latitudes. Note that in general the method applied here allows the strength of each climate  
feedback at equilibrium,  $\lambda_{i,j}^{equil}$ , to be independently assigned for each source of radiative  
338 forcing, (4) and (10), to reflect the different sensitivity of warming to each source of radiative  
forcing (e.g. Hansen et al., 2005; Marvel et al., 2016). However, a full exploration of this  
340 within the WASP model is reserved for future study.

342 Following the methodology of Goodwin et al. (2018), each of the  $10^7$  initial Monte Carlo  
344 prior simulations is then integrated to year 2017 and tested against observational metrics of  
346 surface warming, ocean heat uptake and ocean carbon uptake (Table 2). From the initial  $10^7$   
simulations,  $4.6 \times 10^3$  simulations agree with the observational constraints (Table 2) and are  
extracted to form a final posterior history matched (Williamson et al., 2015) ensemble  
(Figure 4a).

348 This final history matched ensemble of  $4.6 \times 10^3$  simulations has climate feedback strengths  
350 consistent with the CMIP5 ensemble for multiple processes (Table 1), but shows simulated  
warming more tightly constrained by historical observations (Table 2) than for the range 13  
352 CMIP5 models (Figure 4a, compare blue and beige to black; Appendix).

354 The observational constraints for surface warming compare time-average global temperature  
anomalies spanning ten-years or longer (Table 2). Therefore, the observed temperature  
356 anomaly response to volcanic forcing from months to a few years (e.g. Figure 4b, black) has  
not been used to select the final history matched WASP model simulations. The simulated  
358 response of the history-matched WASP model ensemble to a recent volcanic eruption shows  
good agreement to the observed response for the real climate system (Figure 4b, compare  
360 black to blue), both in terms of the magnitude of cooling and the relative timing from the  
AOD perturbation. Although the ensemble simulated cooling is slightly larger than the  
362 observed cooling (Figure 4b), it should be noted that real system includes both the cooling  
effect of the volcanic eruption and the warming effect of the 1991/1992 El Nino event  
364 (Lehner et al., 2016). Accounting for this El Nino event may further improve the model-  
observation agreement. It should also be noted that the simulations record significantly  
366 greater cooling following the Krakatoa eruption in the late 19<sup>th</sup> century than is observed  
(Figure 4a). This is likely due to complexity in the climate system not included within the  
368 WASP model, with observations reflecting both the simultaneous actions of both volcanic  
activity and natural variability, and the complex regional patterns of temperature anomaly.  
370 For example, observations reflect that the 0 to 30°S and 0 to 30°N latitudinal regions both  
saw cooling in the months following the Krakatoa eruption, but the 30 °N to 90 °N region  
372 saw a warming (Robock and Mau, 1995 - Figure 4 therein). The agreement with observations  
of monthly to sub-decadal timescale cooling from a recent volcanic eruption (Figure 4b),  
374 being over a different timescale than the observational constraints (Table 2), provides an  
independent test showing that the time-varying climate feedback approach (10) is functioning  
376 appropriately in the WASP model.

## 378 4. Results

This section presents the results for the constrained distributions of climate feedback and  
380 climate sensitivity over different response timescales, and future warming projections, from  
the history matched WASP ensemble.

382

### 4.1 Constraints on climate feedback and climate sensitivity over time

384 The climate feedback to an imposed radiative forcing alters with the response timescale,  
depending on the processes that act over the different timescales (Figure 2a). In the  
386 experiments carried out here, a wide range of initial climate feedback strengths for different  
processes are used (Figure 2b, gray; Table 1), based on analysis of climate feedback in the  
388 CMIP5 models (Caldwell et al, 2016; Andrews et al., 2015).

390 Observational constraints are then applied to extract the posterior history matched WASP  
ensemble (Table 2), and the range of climate feedback over different response timescales  
392 narrows (Figure 2b, compare blue to gray; Table 1). Starting at the Planck feedback on very  
short timescales, the constrained estimate of climate feedback quickly decreases to  $1.9 \pm 0.3$   
394  $\text{Wm}^{-2} \text{K}^{-1}$  on a response timescale of 0.1 years (Figure 2b, blue), and then slowly decreases  
further to around  $1.5 \pm 0.3 \text{Wm}^{-2} \text{K}^{-1}$  and  $1.3 \pm 0.3 \text{Wm}^{-2} \text{K}^{-1}$  on response timescales of 10 years  
396 and 100 years respectively.

398 The climate sensitivity (in  $^{\circ}\text{C}$ ) is defined as the radiative forcing for a doubling of  $\text{CO}_2$  (in  
 $\text{Wm}^{-2}$ ) divided by the climate feedback (in  $\text{Wm}^{-2} \text{K}^{-1}$ ). Here, this definition is used to convert  
400 the constrained estimate of the climate feedback (Figure 2b, blue) into a constrained estimate  
for the evolution of the climate sensitivity over multiple response timescales (Figure 1; Table  
402 3). The mean constrained estimate of climate sensitivity increases quickly to around  $2^{\circ}\text{C}$   
(ranging from 1.5 to  $2.8^{\circ}\text{C}$  at 95%) on response timescales of 0.1 to 1 year (Figure 1, Table  
404 3), before slowly increasing further to  $2.9^{\circ}\text{C}$  (ranging from 1.9 to  $4.6^{\circ}\text{C}$  at 95 %) over a  
response timescale of 100 years.

406 The 1-year response timescale climate sensitivity identified here is in good agreement with  
408 previous estimates from Earth's current transient energy balance, in which the anthropogenic  
radiative forcing is increasing annually (Figure 1, compare red to dark gray; Lewis and  
410 Curry, 2014; Otto et al., 2013). The 100-year response timescale climate sensitivity identified  
here is in good agreement with previous estimates for the equilibrium sensitivity, either using  
412 an emergent constraint on CMIP5 models or from combining palaeo-climate and historical  
observations (Figure 1, compare blue to light gray; Cox et al., 2018; Goodwin et al., 2018).

#### 414 **4.2 Constraints on the future warming response**

416 The warming projections from the WASP ensemble (Figure 5, blue) are similar to the  
projections from a range of 13 CMIP5 models (Figure 5, beige; Appendix) for both RCP8.5  
418 and RCP4.5 scenarios (Meinshausen et al., 2011). This broad agreement from differing  
approaches, one using complex models and another using a more efficient model with history  
420 matching, provides additional confidence in the future projections (Figure 5, blue and beige).  
The WASP projections do show narrower uncertainty range in future warming than the  
422 CMIP5 models. Possible reasons for this narrowing of future warming in WASP include the  
greater inter-annual and inter-decadal variability inherent in the CMIP5 models, and the  
424 narrower ranges in simulated warming and ocean heat uptake imposed for the present day in  
WASP, due to the tighter observational constraints placed for historic warming and ocean  
426 heat uptake (Table 2; Figure 4). The RCP4.5 scenario does have a reduced chance of  
remaining under  $2^{\circ}\text{C}$  warming for the 21<sup>st</sup> century (less than 1% likelihood) in the  
428 observationally constrained WASP projections, compared to CMIP5 models (Figure 5b,  
compare blue and beige). This is in agreement with the observationally constrained future  
430 warming projections of Goodwin et al. (2018) using a version of the WASP model in which  
the climate feedback is assumed constant in time.

#### 432 **5. Discussion**

434 A modified energy balance equation is presented in which there is no single climate feedback  
applicable to all sources of radiative forcing at time  $t$ ,  $\lambda(t)$ . Instead, surface warming is  
436 calculated using separate the climate feedbacks for each of the  $i$  sources of radiative forcing  
at time  $t$ ,  $\lambda_i(t)$ , that are independently calculated from a set of  $j$  feedback-processes,  $\lambda_{i,j}(t)$ , via

438

$$\Delta T(t) = \left(1 - \frac{N(t)}{R_{total}(t)}\right) \sum_i \left[ \frac{R_i(t)}{\lambda_{Planck} + \sum_j \lambda_{i,j}(t)} \right]. \quad (10)$$

440

Using the ranges of climate feedbacks for different processes analysed for CMIP5 models as a starting point (Table 1; see Caldwell et al. 2016; Andrews et al. 2015), a large ensemble of climate simulations driven by (10) are constructed, and then observational constraints are applied to extract a final history matched ensemble after Goodwin et al. (2018): (Table 2; Figure 4).

446

The final posterior history matched ensemble constrains the climate feedback over multiple timescales (Figure 2b) consistent both with climate feedbacks displayed by the CMIP5 models (Table 1) and with observational constraints of historic warming, heat uptake and carbon uptake (Table 2, Figure 4).

452

Much previous research has gone into constraining the Equilibrium Climate Sensitivity (ECS, in °C), representing the temperature change at equilibrium following a sustained doubling of CO<sub>2</sub> (e.g. IPCC, 2013; Knutti and Rugenstein, 2017). However, in the viewpoint presented here, equation (10), there is no ECS. Instead, the ECS is replaced by a time-evolving climate sensitivity that varies depending on the response timescale (Figure 1; Table 3). The analysis presented here constrains this time-evolving climate sensitivity from sub-annual response timescales up to 10<sup>2</sup> year timescales (Figure 2). However there are additional processes that will alter the climate feedback and climate sensitivity further on longer timescales (e.g. PALAEOSENS, 2012; Rohling et al. 2018; Zeebe, 2013), for example there is an ice-sheet albedo feedback potentially lasting tens of thousands of years. Therefore, the constraint on climate sensitivity for a 10<sup>2</sup> year response timescale presented here (Figure 1, Table 3) should not be considered a final ‘equilibrium’ climate sensitivity, but part of an on-going evolution of climate sensitivity over multiple response timescales (Knutti and Rugenstein, 2017).

466

Consider the seeming inconsistency between previous best-estimates of climate sensitivity (Figure 1), with Earth’s current transient energy balance suggesting a best estimate of around 1.6 to 2 °C (Lewis and Curry, 2014; Otto et al., 2013) and century timescale analysis suggesting best-estimates of around 3 °C (Cox et al., 2018; Goodwin et al., 2018). The combined constraints from the CMIP5 ensemble (Table 1) and observations (Table 3) placed here on the climate sensitivity over response timescales from 0.1, 1 and 10 years (Table 3; Figure 1) are similar to previous estimates of the ECS evaluated from radiative forcing and energy budget constraints (Otto et al, 2013; Lewis & Curry 2014). This similarity is interpreted here as reflecting the short response timescales that the current energy balance of the Earth system has to respond to anthropogenic forcing. Thus, the results for the climate sensitivity over shorter response timescales presented here are consistent with these previous findings (Otto et al. 2013; Lewis and Curry, 2014).

478

The constraint placed here on the climate sensitivity on a response timescale of 100 years (Table 3; Figure 1) agrees very well with two recent estimates of the ECS considering century timescales; one based on the century-timescale response of CMIP5 models with similar autocorrelation lag-1 temperature anomaly properties to the observed climate system (Cox et al., 2018), and another based on a similar history matched approach as used here, but with climate feedback assumed constant over time and an initial prior distribution based on paleoclimate evidence rather than the CMIP5 models (Goodwin et al., 2018).

484

486

488 Thus, this study suggests an interpretation whereby these different previous estimates of  
 490 climate sensitivity are not inconsistent, but merely reflect different response timescales of the  
 492 system (Figure 1). When planning emission pathways to avoid dangerous climate change  
 over the entire 21<sup>st</sup> century, it is appropriate to consider a century response timescale for  
 climate sensitivity. For this purpose, a best estimate 100-year response timescale climate  
 sensitivity of 2.9 °C, with a 66 % range from 2.3 to 3.6 °C, is found (Table 3; Figure 1).

494

This study has used prescriptive input distributions for climate feedback terms based on the  
 CMIP5 models (Table 1), and then applied observational constraints (Table 2) to refine the  
 distributions and constrain the response-timescale evolutions of climate feedback and climate  
 sensitivity (Figures 1 and 2). To adapt the method applied here to use less prescriptive input  
 distributions, such that the output would be independent of the CMIP5 models and based  
 solely on observations, the following issues would need to be considered. Firstly, one would  
 only be able to have a single feedback term for each order of magnitude in timescale. For  
 example the  $\lambda_{\text{WVLR}}$  and  $\lambda_{\text{FastCloud}}$  feedbacks operate over the same order of magnitude  
 timescale and so would need to be combined into a single feedback term. Secondly, one  
 would require an observational constraint generated using (shorter timescale) monthly  
 temperature anomaly data, where the current constraints on surface temperature use a  
 minimum of a ten-year average (Table 2). Such an observational constraint based on monthly  
 temperature anomaly data could possibly be achieved by considering the mean simulated-to-  
 observed difference in the monthly response to a volcanic eruption over a decade (Figure 4b).  
 However, these approaches are beyond the scope of this study and are reserved for future  
 work.

510

Constraining the Earth's climate sensitivity, and understanding its possible response  
 timescale evolution, is critical for reducing uncertainty in future warming projections (e.g.  
 Knutti and Rugenstein, 2015). The history matching method with the WASP model applied  
 in this study not only identifies a probability distribution for climate sensitivity over multiple  
 response timescales (Fig. 1), but also then produces future warming projections using this  
 time-evolving distribution (Fig. 5).

## 518 Appendix

### 520 Appendix A: Changes to the WASP model to allow time-evolving climate feedbacks

To allow time-dependent climate feedbacks in the WASP model, the following alterations are  
 made from the configuration of Goodwin et al. (2018). First, the time-step in the WASP  
 model,  $\delta t$ , is reduced from 1/12<sup>th</sup> of a year in the configuration of Goodwin et al. (2018) to  
 1/48<sup>th</sup> of a year here.

The following equation adjusts the climate feedback to the existing radiative forcing from  $i$ th  
 sources from time  $t$  to time  $t + \delta t$ , considering the  $j$  processes evolve towards their equilibrium  
 feedback values according to their equilibrium timescales,  $\tau_j$  (Table 1),

$$530 \quad \lambda_i(t + \delta t) = \lambda_{\text{Planck}} + \sum_j \left[ \left( \lambda_{i,j}^{\text{equil}} - \lambda_{i,j}(t) \right) \left( 1 - \exp\left( \frac{-\delta t}{\tau_j} \right) \right) \right]. \quad (\text{A1})$$

532 Any additional radiative forcing at time  $t+\delta t$  relative to  $t$  will only operate at the Planck  
 sensitivity, the other feedback terms from the  $j$  processes will be zero in this initial time-step.  
 534 This is expressed by reducing the time-dependent contributions to climate feedback  
 according to the absolute ratio of previous to new radiative forcing,

536

$$\lambda_{i,j}(t+\delta t) = \lambda_{i,j}(t) \left| \frac{R_i(t)}{R_i(t+\delta t)} \right|, \quad (\text{A2})$$

538

noting that (A2) is only applied when the radiative forcing is growing in magnitude,  
 540  $|R_i(t+\delta t)| > |R_i(t)|$ . Note, numerically the absolute value is needed in (A2) because of  
 occasions where  $R_i$  changes sign (e.g. solar forcing) – you don't want to swap the sign of  
 542 lambda for process  $j$ , but reduce it to zero.

544 To calculate the heat imbalance at time  $t$  in WASP,  $N(t)$  in  $\text{Wm}^{-2}$ , the radiative forcing is  
 modulated by the fractional distance from equilibrium of the anthropogenic heat of the  
 546 surface mixed layer,  $H_{mix}(t)$  in J, using (Goodwin, 2016),

$$N(t) = \left( \frac{H_{mix}^{equil}(t) - H_{mix}(t)}{H_{mix}^{equil}(t)} \right) \sum_i R_i(t), \quad (\text{A3})$$

550 where  $H_{mix}^{equil}(t)$  is the eventual heat uptake at equilibrium for the surface mixed layer in J if  
 the radiative forcing at time  $t$  is held constant into the future. Here, allow the climate  
 552 feedback for each source of radiative forcing to evolve independently in time, the equation  
 calculating  $H_{mix}^{equil}(t)$  is modified from the previous form (Goodwin, 2016, equation 3 therein)  
 554 by summing  $R_i/\lambda_i$  for each of the  $i$ -sources of radiative forcing,

$$H_{mix}^{equil}(t) = r_{SST: SAT} V_{mix} c_P \sum_i \frac{R_i(t)}{\lambda_{i,j}(t)}, \quad (\text{A4})$$

558 where  $r_{SST: SAT}$  is the ratio of warming of sea surface temperature to surface air-temperatures at  
 equilibrium,  $V_{mix}$  is the volume of the surface mixed layer and  $c_P$  is the specific heat capacity  
 560 of seawater.

## 562 **Appendix B: Calculating and plotting temperature anomaly.**

For the figures displayed the annual mean temperature anomalies are calculated as follows:  
 564 the GISTEMP record is shown relative to the 1880 to 1900 average, the HadCRUT4 and  
 WASP simulations are shown relative to the 1850 to 1900 average and the CMIP5  
 566 simulations shown relative to the 1861 to 1900 average.

568 The simulated warming ranges of 13 CMIP5 simulations plotted in Figures 4 and 5 include  
 the CanESM2 (Arora et al., 2011), CESM1-BGC (Moore et al., 2013), GFDL-ESM2G  
 570 (Dunne et al., 2013), GFDL-ESM2M (Dunne et al., 2013), HadGEM2-CC (Martin et al.,  
 2011), HadGEM2-ES (Jones et al., 2011), IPSL-CM5A-LR (Dufresne et al., 2013), IPSL-  
 572 CM5A-MR (Dufresne et al., 2013), IPSL-CM5B-LR (Dufresne et al., 2013), MIROC-ESM-  
 CHEM (Watanabe et al., 2011), MIROC-ESM (Watanabe et al., 2011), MPI-ESM-LR Ref.  
 574 50 (Giorgetta et al., 2013) and NorESM1-ME (Tjiputra et al., 2013) models. The shaded

576 regions in Figures 4 and 5 represent the range of annual mean surface warming values from  
the 13 CMIP5 models, using a single realization of each CMIP5 model. The warming is  
578 calculated relative to the 1861-1900 average within each simulation.

### 578 **Acknowledgements**

580 This research was funded by UK NERC grant number NE/N009789/1 and combined UK  
NERC/UK Government Department of BEIS grant number NE/P01495X/1. Comments from  
582 two anonymous reviewers improved the quality of the manuscript.

### 584 **Supplementary Information and data availability**

Two supplementary Information files give the full code for the WASP model described in  
586 this study (Goodwin-ds01.cpp and Goodwin-ds02.cpp). These files are configured to repeat  
all experiments presented in this study, and represent the data for this study.  
588

### 588 **References:**

- 590 Andrews, T and M.J. Webb (2018). The Dependence of Global Cloud and Lapse Rate  
Feedbacks on the Spatial Structure of Tropical Pacific Warming, *Journal of Climate*  
592 <https://doi.org/10.1175/JCLI-D-17-0087.1>
- 594 Andrews, T., J.M. Gregory and M.J. Webb (2015) The Dependence of Radiative Forcing and  
Feedback on Evolving Patterns of Surface Temperature Change in Climate Models, *Journal*  
596 *of Climate* 28, p1630-1648, <https://doi.org/10.1175/JCLI-D-14-00545.1>
- 598 *Armour, K.C., C.M. Bitz and G.H. Roe (2013) Time-Varying Climate Sensitivity from*  
*Regional Feedbacks, Journal of Climate* 26, p4518-4534, [https://doi.org/10.1175/JCLI-D-12-](https://doi.org/10.1175/JCLI-D-12-00544.1)  
600 [00544.1](https://doi.org/10.1175/JCLI-D-12-00544.1)
- 602 Arora, V. K. et al. (2011). Carbon emission limits required to satisfy future representative  
concentration pathways of greenhouse gases. *Geophys. Res. Lett.* 38, L046270.  
604
- Balmaseda, M. A., Mogensen, K. & Weaver, A. T. (2013). Evaluation of the ECMWF  
606 ocean reanalysis system ORAS4. *Q. J. Roy. Meteorol. Soc.* 139, 1132–1161.
- 608 Bourassa, A.E., A. Robock, W.J. Randel, T. Deshler, L.A. Reiger, N.D. Lloyd, E.J.  
Llewellyn & D.A. Degenstein (2012). Large volcanic aerosol load in the stratosphere linked  
610 to Asian monsoon transport. *Science* 337, 78-81, [doi:10.1126/science.1219371](https://doi.org/10.1126/science.1219371).
- 612 Caldwell, P.M., M.D. Zelinka, K.E. Taylor, and K. Marvel (2016). Quantifying the Sources  
of Intermodel Spread in Equilibrium Climate Sensitivity, *Journal of Climate* 29, 513-524,  
614 DOI:10.1175/JCLI-D-15-0352.1.
- 616 Cheng, L. et al. (2017). Improved estimates of ocean heat content from 1960 to 2015. *Sci.*  
*Adv.* 3, e1601545.  
618
- Cox, P.M., C. Huntingford & M.S. Williamson (2018). Emergent constraint on equilibrium  
620 climate sensitivity from global temperature variability, *Nature* 553, 319–322,  
doi:10.1038/nature25450.
- 622
- Dufresne, J. L. et al. (2013). Climate change projections using the IPSL-CM5 Earth system  
624 model: from CMIP3 to CMIP5. *Climate Dynamics* 40, 2123–2165.

626 Dunne, J. P. et al. (2013). GFDLs ESM2 global coupled climate carbon Earth system models.  
 Part II: Carbon system formulation and baseline simulation characteristics. *J. Clim.* 26, 2247–  
 628 2267.

630 Frölicher TL, M. Winton & J.L. Sarmiento (2014) Continued global warming after CO2  
 emissions stoppage. *Nature Climate Change* 4:40–44  
 632

Geoffroy O. et al. (2013) Transient climate response in a two-layer energy-balance model.  
 Part II: representation of the efficacy of deep-ocean heat uptake and validation for CMIP5  
 634 AOGCMs. *J. Clim* 26:1859–1876

636

Giese, B. S. & S. Ray. (2011). El Niño variability in simple ocean data assimilation (SODA),  
 638 1871–2008. *J. Geophys. Res.* 116, C02024.

640 Giorgetta, M. A. et al. (2013). Climate and carbon cycle changes from 1850 to 2100 in MPI-  
 ESM simulations for the Coupled Model Intercomparison Project phase 5: climate changes in  
 642 MPI-ESM. *J. Adv. Model. Earth Syst.* 5, 572–597.

644 GISS Surface Temperature Analysis (GISTEMP) (NASA Goddard Institute for Space  
 Studies, accessed 5th April 2018); <https://data.giss.nasa.gov/gistemp/>  
 646

Good, S. A., M.J. Martin, & N.A. Rayner (2013). EN4: quality controlled ocean temperature and  
 648 salinity profiles and monthly objective analyses with uncertainty estimates. *J. Geophys.  
 Res. Ocean.* 118, 6704–6716.

650

Goodwin, P., A. Katavouta, V.M. Roussenov, G.L. Foster, E.J. Rohling and R.G. Williams,  
 652 (2018) Pathways to 1.5 and 2 °C warming based on observational and geological constraints,  
*Nature Geoscience* 11, 102-107, doi:10.1038/s41561-017-0054-8.

654

Goodwin, P. (2016) How historic simulation-observation discrepancy affects future warming  
 656 projections in a very large model ensemble, *Climate Dynamics*, CLDY-D-15-00368R2, doi:  
 10.1007/s00382-015-2960-z.

658

Goodwin, P., R.G. Williams and A. Ridgwell (2015), Sensitivity of climate to cumulative  
 660 carbon emissions due to compensation of ocean heat and carbon uptake, *Nature Geoscience*  
 8, p29-34. doi:10.1038/ngeo2304.

662

Gregory, J.M. and T. Andrews (2016), Variation in climate sensitivity and feedback  
 664 parameters during the historical period, *Geophysical Research Letters*, Volume 43, Issue  
 8, pages 3911–3920.

666

Gregory, J.M., T. Andrews, P. Good, T. Mauritsen, & P.M. Forster (2016) Small global-mean  
 668 cooling due to volcanic radiative forcing, *Climate Dynamics* 47, 3979–3991, DOI  
 10.1007/s00382-016-3055-1.

670

Gregory, J. M., W. J. Ingram, M. A. Palmer, G. S. Jones, P. A. Stott, R. B. Thorpe, J. A.  
 672 Lowe, T. C. Johns, and K. D. Williams (2004), A new method for diagnosing radiative  
 forcing and climate sensitivity, *Geophys. Res. Lett.*, 31, L03205,  
 674 doi:10.1029/2003GL018747.

676 Hansen, J., M. Sato, R. Ruedy, L. Nazarenko, A. Lacis, G. A. Schmidt, G. Russell, et al.  
 (2005) Efficacy of climate forcings, *J. Geophys. Res.*, 110, D18104,  
 678 doi:10.1029/2005JD005776.

680 Hansen, J., S. Ruedy, M. Sato & K. Lo (2012). Global surface temperature change. *Rev.*  
*Geophys.* 48, RG4004.

682 Huang, B. et al. (2015) Extended Reconstructed Sea Surface Temperature Version 4  
 684 (ERSST.v4). Part I: Upgrades and intercomparisons. *J. Clim.* 28, 911–930.

686 IPCC (2013) *Climate Change 2013: The Physical Science Basis* (eds Stocker, T. F. et  
 al.) (Cambridge Univ. Press, Cambridge, 2013).

688 Jones, C. D. et al. (2011). The HadGEM2-ES implementation of CMIP5 centennial  
 690 simulations. *Geosci. Model. Dev.* 4, 543–570.

692 Kennedy, J. J., Rayner, N. A., Smith, R. O., Saunby, M. & Parker, D. E. (2011). Reassessing  
 biases and other uncertainties in sea-surface temperature observations measured in situ since  
 694 1850. Part 2: Biases and homogenisation. *J. Geophys. Res.* 116, D14104.

696 Knutti, R. and M.A.A. Rugenstein (2015) Feedbacks, climate sensitivity and the limits of  
 linear models. *Phil. Trans. R. Soc. A* **373**: 20150146.  
 698 <http://dx.doi.org/10.1098/rsta.2015.0146>

700 Knutti, R., M.A.A. Rugenstein and G.C. Hegerl (2017) Beyond equilibrium climate  
 sensitivity, *Nature Geoscience* 10, 727-736, DOI:10.1038/ngeo3017.

702 Lehner, F., A. P. Schurer, G. C. Hegerl, C. Deser, and T. L. Frölicher (2016), The importance  
 704 of ENSO phase during volcanic eruptions for detection and attribution, *Geophys. Res. Lett.*,  
 43(6), doi:10.1002/2016GL067935.

706 Levitus, S. et al. (2012). World ocean heat content and thermosteric sea level change (0–2000  
 708 m), 1955–2010. *Geophys. Res. Lett.* 39, 10.

710 Lewis, N. & J.A. Curry (2014) The implications for climate sensitivity of AR5 forcing and  
 heat uptake estimates, *Climate Dynamics* 45, 1009-1023.

712 Martin, G. M. et al. (2011). The HadGEM2 family of Met Office Unified Model climate  
 714 configurations. *Geosci. Model. Dev.* 4, 723–757.

716 Meinshausen, M. et al. (2011). The RCP greenhouse gas concentrations and their extensions  
 from 1765 to 2300. *Climatic Change* 109, 213–241.

718 Moore, J., Lindsay, K., Doney, S., Long, M. & Misumi, K. (2013). Marine ecosystem  
 720 dynamics and biogeochemical cycling in the Community Earth System Model  
 [CESM1(BGC)]: comparison of the 1990s with the 2090s under the RCP4.5 and RCP8.5  
 722 scenarios. *J. Clim.* 26, 9291–9312.

724 Morice, C. P., Kennedy, J. J., Rayner, N. A. & Jones, P. D. (2012). Quantifying uncertainties  
726 in global and regional temperature change using an ensemble of observational estimates: the  
HadCRUT4 dataset. *J. Geophys. Res.* 117, D08101.

728 Myhre, G., et al. (2013) Anthropogenic and Natural Radiative Forcing Supplementary  
730 Material. In: *Climate Change 2013: The Physical Science Basis. Contribution of Working  
732 Group I to the Fifth Assessment Report of the Intergovernmental Panel on Climate Change*  
[Stocker, T.F., D. Qin, G.-K. Plattner, M. Tignor, S.K. Allen, J. Boschung, A. Nauels, Y. Xia,  
V. Bex and P.M. Midgley (eds.)].

734 Otto, A., F.E.L. Otto, O. Boucher, J. Church, G. Hegerl, P.M. Forster, N.P. Gillett, et al.  
736 (2013) Energy budget constraints on climate response, *Nature Geoscience* 6, 415-416.

738 PALAEOSENS (2012). Making sense of palaeoclimate sensitivity. *Nature* 491, 683–691.

740 Paynter, D., T.L. Frölicher, L.W. Horowitz, and L.G. Silvers (2018), Equilibrium Climate  
742 Sensitivity Obtained From Multimillennial Runs of Two GFDL Climate Models, *J. Geophys.  
744 Res. Atmos.*, 123(4), 1921-1941, doi:10.1002/2017JD027885.

746 Robock, A., & J. Mau (1995) The Volcanic Signal in Surface Temperature Observations,  
748 *Journal of Climate*, 8, 1086-1102.

746 Rohling, E.J., G. Marino, G.L. Foster, P.A. Goodwin, A.S. von der Heydt, P. Köhler (2018)  
748 Comparing Climate Sensitivity, Past and Present, *Annual Review of Marine Science*,  
750 10, pp.261–288. [http://www.annualreviews.org/doi/full/10.1146/annurev-marine-121916-  
750 063242](http://www.annualreviews.org/doi/full/10.1146/annurev-marine-121916-063242)

752 Senior, C., and J. F. Mitchell (2000), The time-dependence of climate sensitivity, *Geophys.  
754 Res. Lett.*, 27(17), 2685-2688, doi:10.1029/2000GL011373.

754 Smith, T. M., R.W. Reynolds, T.C. Peterson & J. Lawrimore (2008). Improvements to  
756 NOAA’s historical merged land–ocean surface temperature analysis (1880–2006). *Journal of  
758 Climate* 21, 2283–2296.

758 Smith, D. M. et al. (2015). Earth’s energy imbalance since 1960 in observations and CMIP5  
760 models. *Geophys. Res. Lett.* 42.4, 1205–1213.

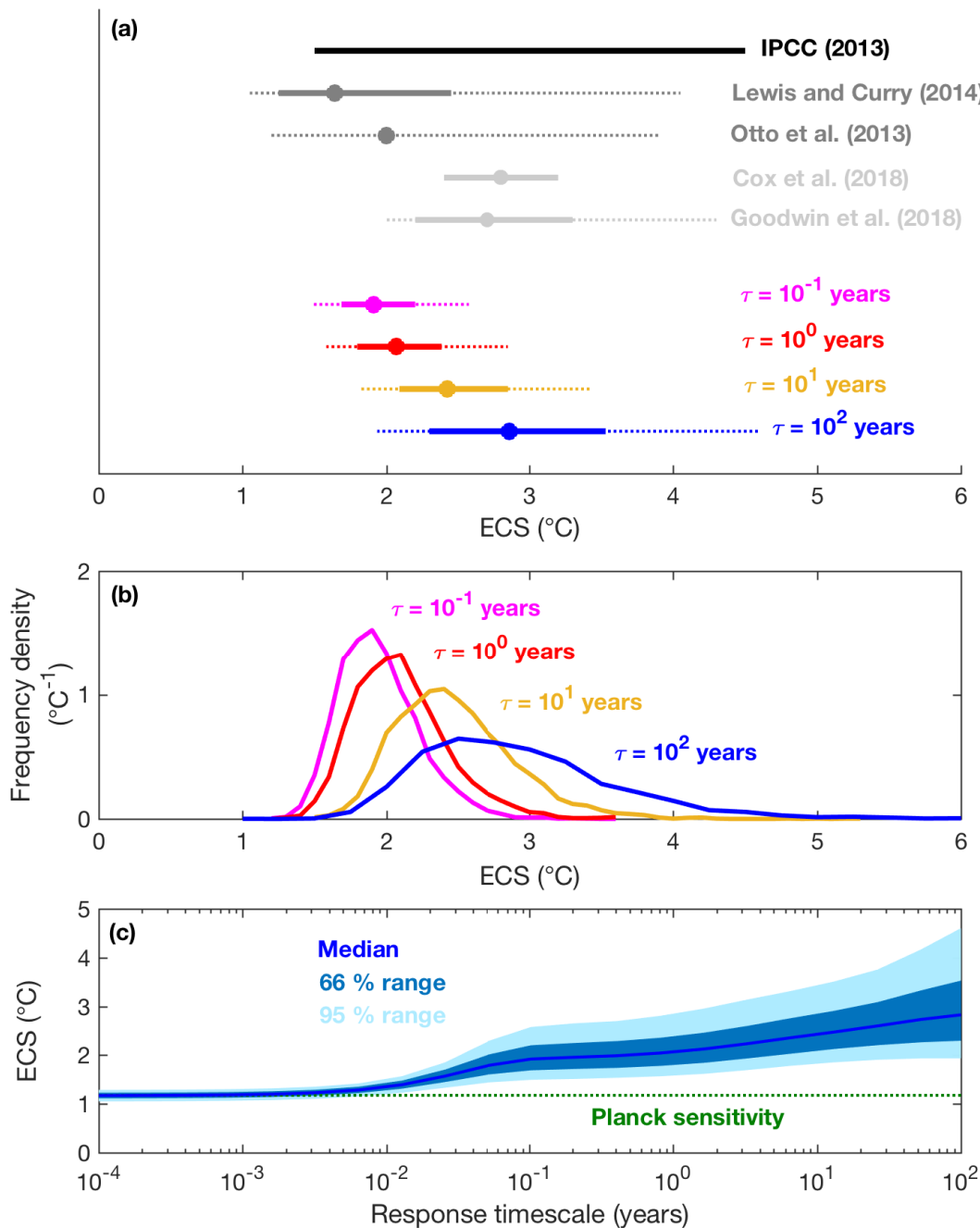
762 Tjiputra, J. F. et al. (2013). Evaluation of the carbon cycle components in the Norwegian  
764 Earth System Model (NorESM). *Geosci. Model. Dev.* 6, 301–325.

764 Vose, R. S. et al. (2012). NOAA’s merged land–ocean surface temperature analysis. *Bull.  
766 Am. Meteorol. Soc.* 93, 1677–1685.

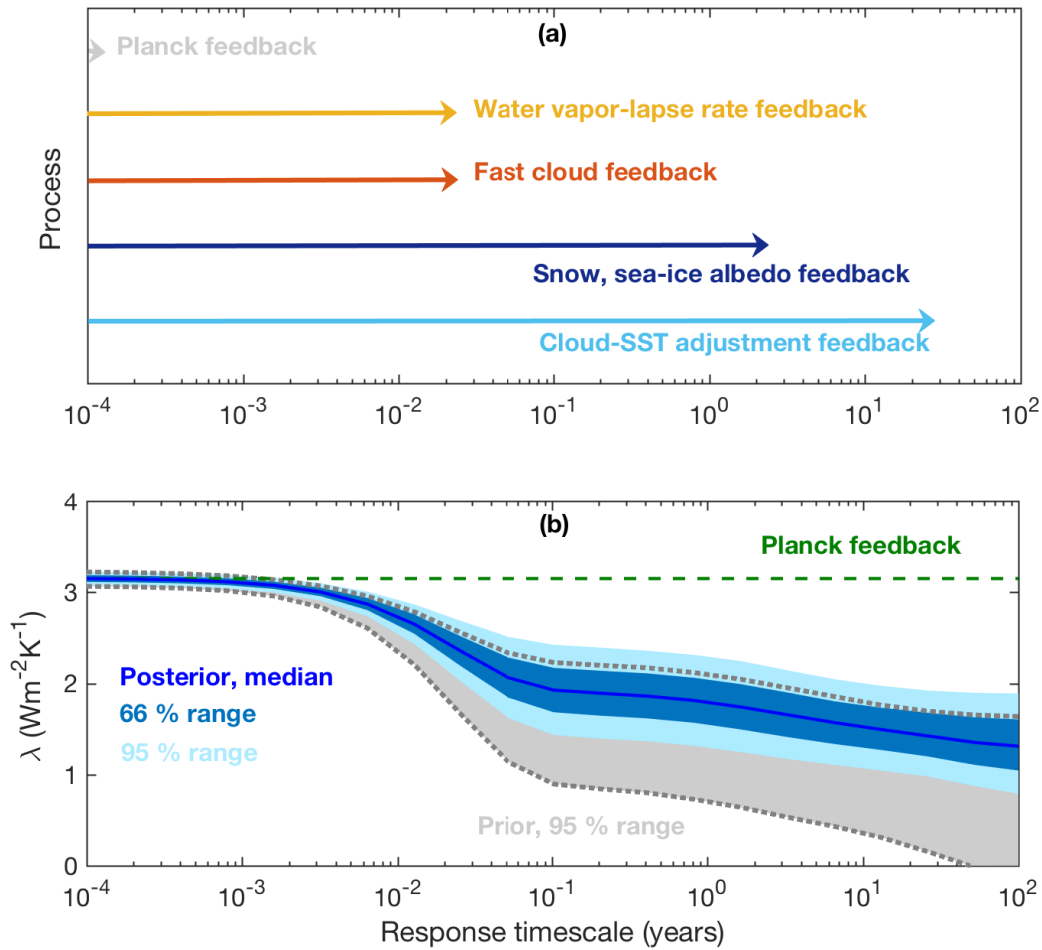
768 Watanabe, S. et al. (2011). MIROC-ESM 2010: model description and basic results of  
770 CMIP5-20c3m experiments. *Geosci. Model. Dev.* 4, 845–872.

772 Williams, K. D., W. J. Ingram, and J. M. Gregory (2008), Time Variation of Effective  
Climate Sensitivity in GCMs, *J. Clim.*, 21(19), 5076-5090, doi:10.1175/2008JCLI2371.1.

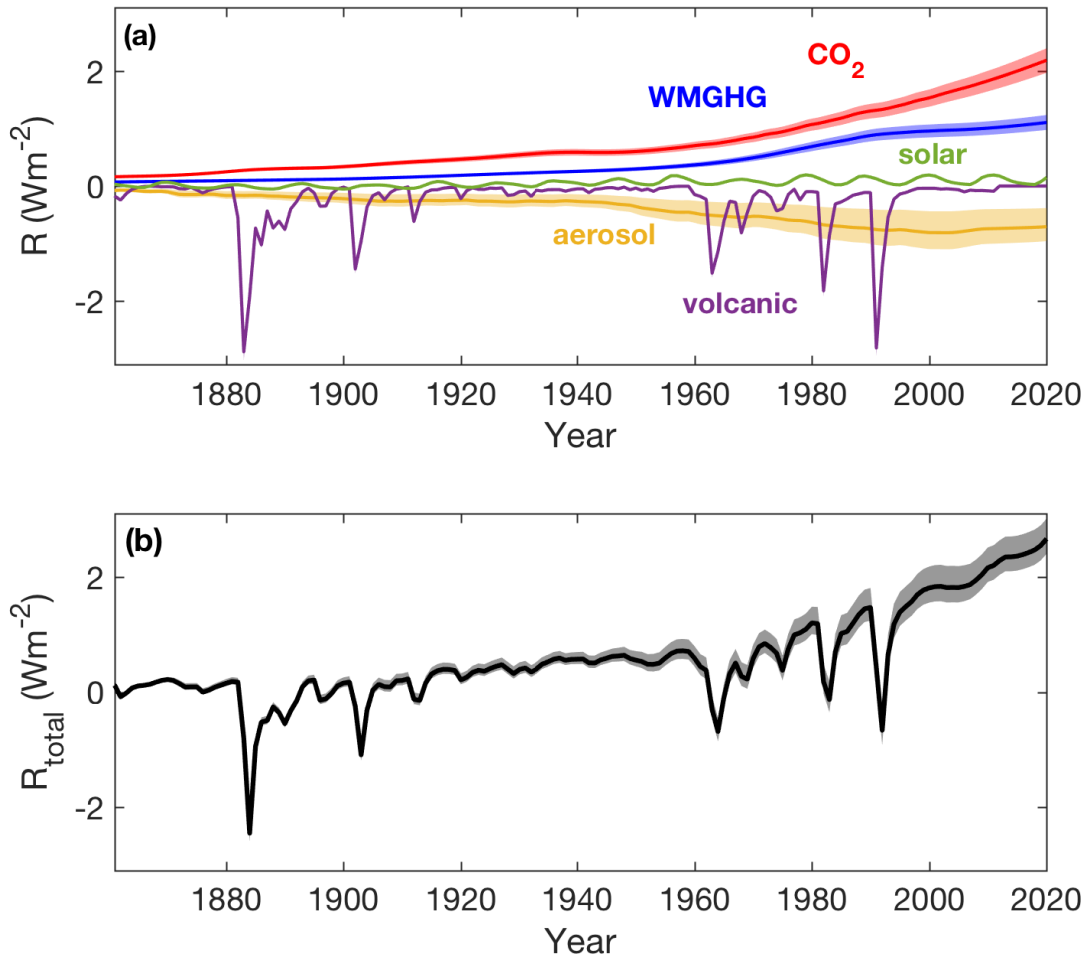
- 774 Williamson, D., A.T. Blaker, C. Hampton, & J. Salter (2015). Identifying and removing  
structural biases in climate models with history matching. *Climate Dynamics* 45, 1299-1324.  
DOI:10.1007/s00382-014-2378-z.
- 776
- 778 Winton M, Takahashi K, Held I (2010) Importance of ocean heat uptake efficacy to transient  
climate change. *Journal of Climate* 23:2333–2344
- 780 Zeebe, R.E. Time-dependent climate sensitivity and the legacy of anthropogenic greenhouse  
gas emissions, *Proc. Natl. Acad. Sci.*, vol. 110 no. 34, 13739–13744, doi:  
782 10.1073/pnas.1222843110



786 **Figure 1: The constrained evolution of climate sensitivity over multiple response**  
 788 **timescales.** (a) Estimates of the climate sensitivity ( $^{\circ}\text{C}$ ) from multiple studies (black and  
 789 gray) compared to the posterior history matched WASP ensembles in this study evaluated  
 790 over multiple response timescales ranging from  $10^{-1}$  to  $10^2$  years (colors). Dots are best  
 791 estimates (using median from distributions for this study), thick solid lines are 66 % ranges  
 792 and dotted lines are 95 % ranges. (b) The frequency density distributions of climate  
 793 sensitivity in the posterior history matched WASP ensembles over multiple response  
 794 timescales. (c) The climate sensitivity ( $^{\circ}\text{C}$ ) over multiple response timescales in the posterior  
 history matched WASP ensemble (blue, lines and shading show median and uncertainty  
 ranges).



798 **Figure 2: Time evolution of climate feedback over multiple timescales.** (a) Schematic of  
 800 different climate feedback processes considered in this study, and their characteristic  
 802 response timescales. (b) The climate feedback over different response timescales in the initial  
 804 prior model ensemble (grey: shaded area and dotted lines, showing 95% range) and in the  
 final posterior history matched ensemble (blue, line is median, dark blue shading is 66%  
 range, light blue shading is 95 % range). Also shown for comparison is the Planck sensitivity  
 (green).



806

808

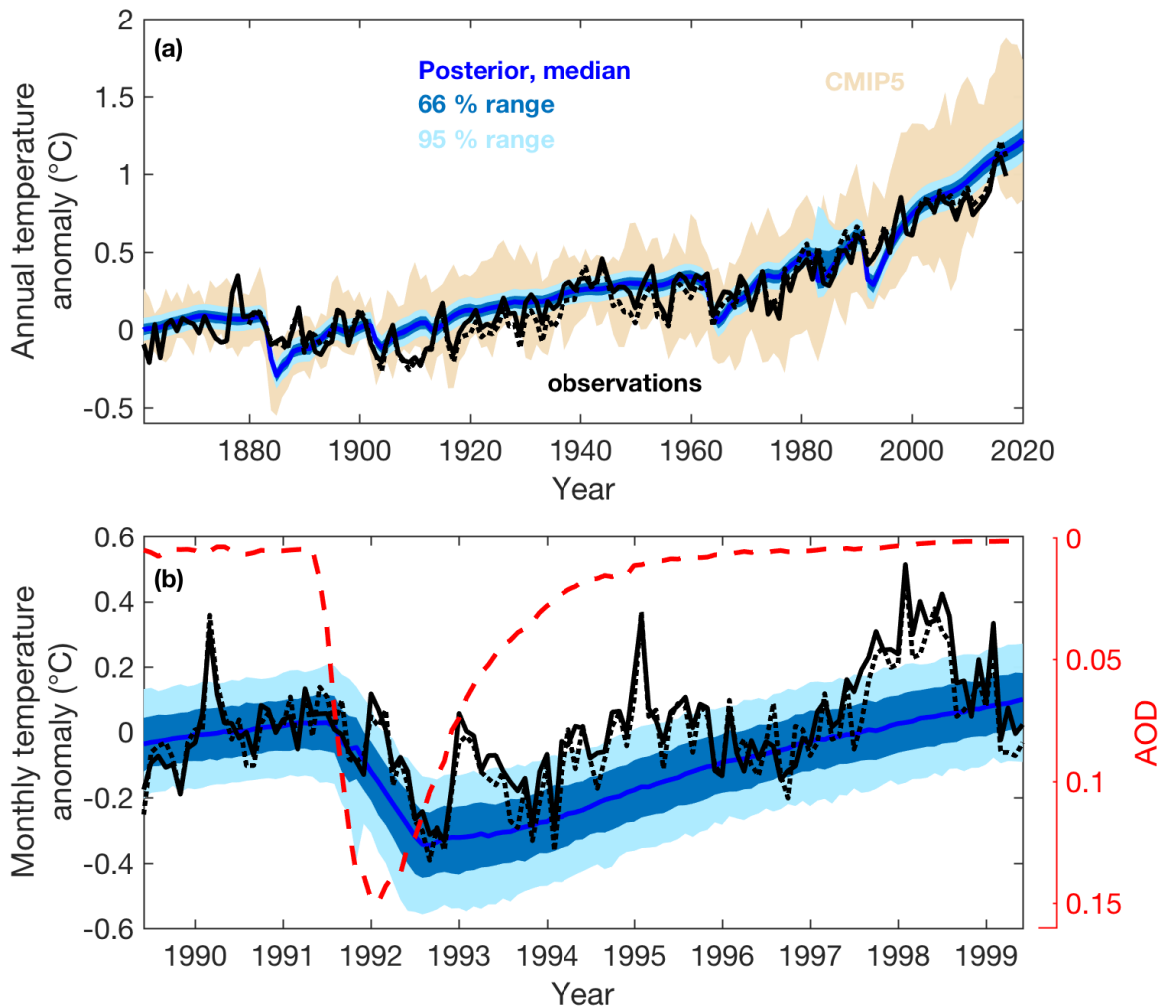
810

812

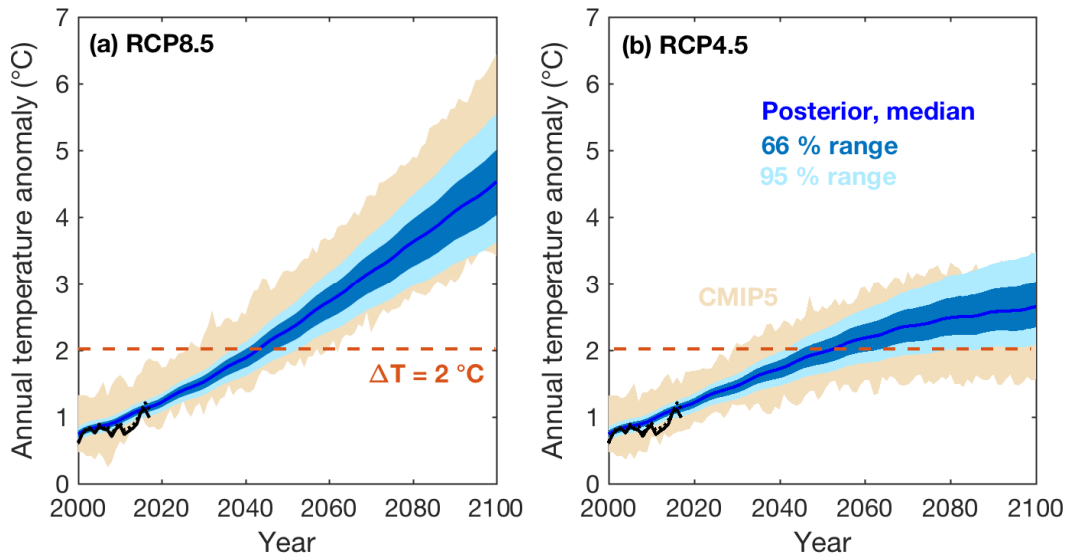
814

816

**Figure 3. Applied radiative forcing over time.** (a) Radiative forcing over time from multiple sources in the posterior history matched model ensemble, showing median (line) and 95% range (shading). The sources of radiative forcing are: atmospheric  $\text{CO}_2$  (red), Well mixed Greenhouse Gasses (WMGHG) other than  $\text{CO}_2$  (blue), tropospheric aerosols (orange), volcanic stratospheric aerosols (purple), and solar forcing (green). (b) The total radiative forcing from all sources,  $R_{\text{total}}$ , over time in the posterior history matched model ensemble (line is median, shaded area is 95% range). All radiative forcings are annually smoothed with the exception of volcanic aerosols, which have a monthly resolution.



818 **Figure 4. Observed and simulated temperature anomaly over time.** (a) Annual mean  
 820 temperature anomaly from 1861 to 2020. Shown are observations to (black: solid line is  
 822 HadCRUT4 from 1861-2017, dotted line is GISTEMP from 1880 to 2017) and simulated  
 824 temperature anomaly from the posterior WASP history matched ensemble of simulations  
 826 with modified energy balance (blue, lines and shading as Figure 1b), and from 13 CMIP5  
 828 models (beige shading showing range). All annual temperature anomalies are shown relative  
 830 to the pre-1900 average (Appendix B). (b) Monthly temperature anomaly before and after the  
 eruption of Mt. Pinatubo from observations (black, as panel a) and the posterior history  
 matched WASP ensemble simulations (blue, as panel a), and the AOD (red). Both observed  
 and simulated monthly temperature anomalies are shown relative to the 2-year average prior  
 to the eruption of Mt. Pinatubo.



832

834

836

838

840

**Figure 5: Warming over the 21<sup>st</sup> century.** Future warming projections from the posterior history matched WASP ensemble (blue, line and shading as figure 1b) and a range of 13 CMIP5 Earth system models (beige shading showing range; see Appendix) for (a) RCP8.5 and (b) RCP4.5 scenarios. Also shown are observed warming from 2000 to 2017 (black lines: solid is HadCRUT4, dotted is GISTEMP).

Feedback process	Equilibrium feedback input distribution	e-folding adjustment timescale input distribution	Posterior climate feedback (mean and standard deviation)
Planck Feedback <sup>a</sup> , $\lambda_{Planck}$	Random-normal: $\mu = 3.15 \text{ Wm}^{-2}\text{K}^{-1}$ $\sigma = 0.04 \text{ Wm}^{-2}\text{K}^{-1}$	Instantaneous	$\mu = 3.15 \text{ Wm}^{-2}\text{K}^{-1}$ $\sigma = 0.04 \text{ Wm}^{-2}\text{K}^{-1}$
Combined water vapour-lapse rate feedback <sup>a</sup> , $\lambda_{WVLR}$	Random-normal: $\mu = -1.15 \text{ Wm}^{-2}\text{K}^{-1}$ $\sigma = 0.09 \text{ Wm}^{-2}\text{K}^{-1}$	Random-normal: $\mu = 8.9 \text{ days}$ $\sigma = 0.4 \text{ days}$	$\mu = -1.13 \text{ Wm}^{-2}\text{K}^{-1}$ $\sigma = 0.09 \text{ Wm}^{-2}\text{K}^{-1}$
Fast cloud feedback <sup>a</sup> (initial transient SST patterns), $\lambda_{FastClouds}$	Random-normal: $\mu = -0.43 \text{ Wm}^{-2}\text{K}^{-1}$ $\sigma = 0.33 \text{ Wm}^{-2}\text{K}^{-1}$	Random-normal: $\mu = 8.9 \text{ days}$ $\sigma = 0.4 \text{ days}$	$\mu = -0.11 \text{ Wm}^{-2}\text{K}^{-1}$ $\sigma = 0.26 \text{ Wm}^{-2}\text{K}^{-1}$
Snow + sea-ice albedo climate feedback <sup>a</sup> , $\lambda_{albedo}$	Random-normal: $\mu = -0.37 \text{ Wm}^{-2}\text{K}^{-1}$ $\sigma = 0.10 \text{ Wm}^{-2}\text{K}^{-1}$	Random: Min. = 0.5 years, Max. = 5.0 years	$\mu = -0.34 \text{ Wm}^{-2}\text{K}^{-1}$ $\sigma = 0.10 \text{ Wm}^{-2}\text{K}^{-1}$
Cloud – spatial SST adjustment feedback <sup>b</sup> , $\lambda_{SlowCloud}$	Random-normal: $\mu = -0.47 \text{ Wm}^{-2}\text{K}^{-1}$ $\sigma = 0.30 \text{ Wm}^{-2}\text{K}^{-1}$	Random: Min. = 20 years, Max. = 45 year.	$\mu = -0.27 \text{ Wm}^{-2}\text{K}^{-1}$ $\sigma = 0.28 \text{ Wm}^{-2}\text{K}^{-1}$

842 **Table 1: Time-evolving climate feedbacks in the WASP model.** All input distributions are  
844 identical for the different sources of radiative forcing, except that for volcanic radiative  
845 forcing the snow + sea-ice albedo feedback is reduced to 20% of the value for other sources.  
846 <sup>a</sup> Input distribution taken from the CMIP5 models as analyzed by Caldwell et al. (2016).  
<sup>b</sup> Input distribution taken from the CMIP5 models as analyzed by Andrews et al. (2015).

<b>Observational constraint</b>	<b>Observation-consistent range</b>	<b>Comment/References</b>	<b>Posterior 95 % range</b>
Global mean temperature anomaly, 1986-2005 relative to 1850-1900	0.55 to 0.67 °C	Constraint amended from 2003-2012 period in Goodwin et al. (2018) to 1986-2005 period here, so that the final time-average includes a significant volcanic eruption. Range based on 90% observational range from IPCC (2013).	0.55 to 0.67 °C
Global mean temperature anomaly, 2007-2016 relative to 1971-1980	0.56 to 0.69 °C	Constraints and ranges as used in Goodwin et al. (2018). Based on: (Morice et al. 2012; GISTEMP, 2018; Hansen et al., 2010; Smith et al., 2008; Vose et al., 2012)	0.57 to 0.69 °C
Global mean temperature anomaly, 2007-2016 relative to 1951-1960	0.54 to 0.78 °C		0.63 to 0.76 °C
Global mean sea-surface temperature anomaly, 2003-2012 relative to 1850-1900	0.56 to 0.68 °C	Constraint and range as used in Goodwin et al. (2018). Based on (Kennedy et al., 2011; Huang et al., 2015)	0.56 to 0.68 °C
Whole ocean heat content anomaly, 2010 relative to 1971	117 to 332 ZJ	Constraints and ranges as used in Goodwin et al. (2018). Based on (Levitus et al., 2012; Giese et al., 2011; Balmaseda et al., 2013; Good et al., 2013; Smith et al., 2018; Cheng et al., 2017)	152 to 337 ZJ
Upper 700m ocean heat content anomaly, 2010 relative to 1971	98 to 170 ZJ		103 to 171 ZJ
Terrestrial carbon uptake, 2011 relative to preindustrial	70 to 250 PgC	Constraint and range as used in Goodwin et al. (2018). Based on IPCC (2013)	95 to 253 PgC
Rate of terrestrial carbon uptake, 2000 to 2009	1.4 to 3.8 PgC yr <sup>-1</sup>	Constraint and range as used in Goodwin et al. (2018). Based on IPCC (2013)	1.3 to 3.6 PgC yr <sup>-1</sup>
Ocean carbon uptake, 2011 relative to preindustrial	125 to 185 PgC	Constraint and range as used in Goodwin et al. (2018). Based on IPCC (2013)	126 to 181 PgC

848 **Table 2: Observational constraints and posterior simulated ranges.** All constraints  
850 represent 90 or 95 % uncertainty ranges in the observed quantities. See Goodwin et al. (2018)  
for details.

852

<b>Response timescale, <math>\tau</math></b>	<b>Median Climate Sensitivity</b>	<b>66% range in Climate Sensitivity</b>	<b>95 % range in Climate Sensitivity</b>
0.1 years	1.9 °C	1.7 to 2.2 °C	1.5 to 2.6 °C
1 years	2.1 °C	1.8 to 2.4 °C	1.6 to 2.8 °C
10 years	2.4 °C	2.1 to 2.9 °C	1.8 to 3.4 °C
100 years	2.9 °C	2.3 to 3.5 °C	1.9 to 4.6 °C

**Table 3: Constrained climate sensitivity estimates for multiple response timescales.**

854